Towards improved urban flood detection using Sentinel-1: dependence of the ratio of post- to pre-flood double scattering cross-sections on building orientation

Article

Published Version

Creative Commons: Attribution 4.0 (CC-BY)

open access

Mason, D. C. ORCID: https://orcid.org/0000-0001-6092-6081, Dance, S. L. ORCID: https://orcid.org/0000-0003-1690-3338 and Cloke, H. L. ORCID: https://orcid.org/0000-0002-1472-868X (2023) Towards improved urban flood detection using Sentinel-1: dependence of the ratio of post- to pre-flood double scattering cross-sections on building orientation. Journal of Applied Remote Sensing, 17 (1). 016507. ISSN 1931-3195 doi: 10.1117/1.JRS.17.016507 Available at https://centaur.reading.ac.uk/110425/

www.reading.ac.uk/centaur

CentAUR

Central Archive at the University of Reading

Reading's research outputs online

Toward improved urban flood detection using Sentinel-1: dependence of the ratio of post- to preflood double scattering cross sections on building orientation

David C. Mason[a],* **Sarah L. Dance[b,c,d] and Hannah L. Cloke[a,b,e,f]**
aUniversity of Reading, Department of Geography and Environmental Science, Reading, United Kingdom
bUniversity of Reading, Department of Meteorology, Reading, United Kingdom
cUniversity of Reading, Department of Mathematics and Statistics, Reading, United Kingdom
dNational Centre for Earth Observation, Reading, United Kingdom
eUppsala University, Department of Earth Sciences, Uppsala, Sweden
fCentre for Natural Hazards and Disaster Science, Uppsala, Sweden

Abstract. High-resolution synthetic aperture radar (SAR) sensors are now commonly used for flood detection. Automated detection tends to be limited to rural areas owing to the complicated backscattering mechanisms occurring in urban areas. Flooding can be identified in urban areas by searching for increased SAR backscatter in a postflood image due to double scattering between water and adjacent buildings, compared with a preflood image where double scattering is between unflooded ground and buildings. For co-polarized data, if φ is the angle between the building wall and the satellite direction of travel, double scattering is strongest for $\varphi = 0$ deg and falls off as φ increases. Theoretical studies estimating the ratio of flooded-to-unflooded double scatterer (DS) radar cross section (RCS) using X-band SAR data, found that the ratio was high at $\varphi = 0$ deg but only small at $\varphi > 10$ deg. Ostensibly, this implies that few DSs might be detected in an urban area. However, experiments on real images have called into question the veracity of the modeling. We describe an empirical study to examine the relationship between the flooded-to-unflooded DS RCS ratio and φ in Sentinel-1 (S-1) C-band data. We use high-resolution light detection and ranging and aerial photographs so that φ can be measured accurately and is based on S-1 images from flood events that occurred in the United Kingdom during the storms of winter 2019 to 2020. Results indicate that vertical–vertical polarization is better than vertical–horizontal at distinguishing flooded from unflooded DS; that the theoretical model used underestimates the number of DS with high RCS ratios in the φ range 10 deg to 30 deg; and that sufficient DS ground heights can be determined to estimate an accurate local average flood level, although in high density housing there are less of these due to the presence of adjacent buildings. © *The Authors. Published by SPIE under a Creative Commons Attribution 4.0 International License. Distribution or reproduction of this work in whole or in part requires full attribution of the original publication, including its DOI.* [DOI: 10.1117/1.JRS.17.016507]

1 Introduction

Floods are a major natural hazard in many parts of the world and are likely to become more frequent and severe in the future due to climate change and growing urbanization.[1] While the majority of a flooded area may often be rural, it is in the urban areas that the risks to people and property are highest.

High-resolution synthetic aperture radar (SAR) rather than visible band sensors are now commonly the sensors of choice for flood detection, because of the ability of SAR to penetrate the cloud that is often present during flooding and to image at night as well as during the day.

---

*Address all correspondence to David C. Mason, d.c.mason@reading.ac.uk

The Sentinel-1 (S-1) constellation is particularly attractive for flood studies, as it provides open access, processed, and geo-registered data in near real-time on a global basis.[2] Important uses of the flood extents from near real-time SAR images are for operational flood incident management[3] and assimilation into urban flood inundation models.[4–7]

In rural areas, floodwater generally appears dark in a SAR image due to specular reflection from the water surface away from the antenna, provided there is no significant surface water turbulence. A substantial amount of research has been carried out on automated flood detection in rural areas. For a discussion of the literature, see Refs. 8 and 9. This work has culminated in the recent launch by the Copernicus Emergency Management Service of the Global Flood Monitoring (GFM) product, which produces near real-time flood extents using an ensemble of methods for all S-1 images acquired.[10,11]

Unfortunately, SAR flood detection algorithms designed to work in rural areas tend not to work so well in urban areas. In urban areas, substantial areas of ground surface may not be visible to the SAR due to radar shadowing and layover caused by buildings. In addition, the image may be confused by double scattering between ground surfaces and adjacent buildings. As a result, automation of urban flood detection using SAR has lagged behind rural flood detection. Despite this, several studies have now been made. Techniques employed include analysis of backscatter in a postflood SAR image,[12–16] analysis of change in backscatter between pre- and postflood SAR images,[17] use of coherence as well as backscatter in pre- and postflood SAR images,[2,18–21] and time series analysis of SAR images.[22]

Reference 23 recently developed a method for detecting flooding at high resolution in urban areas using S-1 SAR and WorldDEM digital surface model (DSM) data. The method is a change detection technique that estimates flood levels using pre- and postflood images. It searches for increased SAR backscatter in the postflood image due to double scattering between water and adjacent buildings, compared with that in the preflood image where double scattering is between unflooded ground and adjacent buildings. The double scattering is caused by the corner reflector formed from the wall of a building facing the satellite and the ground in front of the wall (Fig. 1). The effect is particularly apparent for building walls that are roughly parallel to the satellite direction of travel.[24] For co-polarized data, if φ is the angle between the wall and the satellite direction of travel, double scattering is strongest for $\varphi = 0$ deg, and falls off as φ increases. It also depends on the wall height and length, the depth of flooding, the roughness of the ground surface, and the complex dielectric constants of the building wall and ground surface.

Reference 18 used the theoretical model of Ref. 25 to estimate the post- to preflood radar cross section (RCS) ratio for double scatterers (DSs) using very high-resolution horizontal–horizontal (HH) polarized X-band SAR data, and found that it reduced rapidly from 11.5 dB at $\varphi = 0$ deg to no more than 3.5 dB at $\varphi > 10$ deg. Reference 18 concluded that, for X-band data, the increase of the double scattering due to floodwater was not very high if buildings were
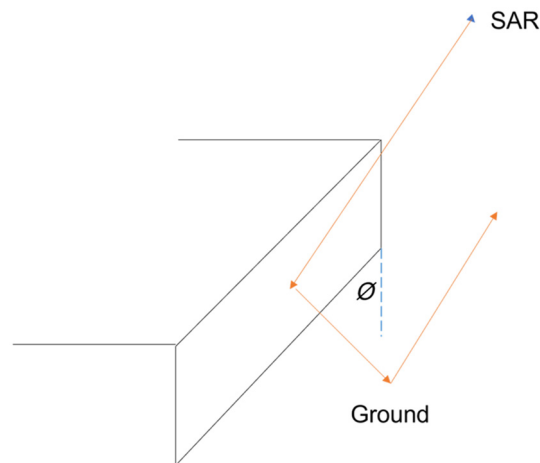

Fig. 1 Double scattering between wall and ground (SAR flying into paper) (φ = angle between wall and satellite flight direction).

not roughly parallel to the SAR flight direction. The modeling assumed isolated buildings, and in a complex urban environment it was thought that any increase would be further masked by the effects of adjacent buildings. This implies a possible limitation in methods similar to that of Ref. 23, since if the falloff with increasing φ is very rapid, this could reduce the number of DSs that could be distinguished as flooded or unflooded in the postflood image.

Reference 25 considered the reliability of their theoretical model for predicting double scattering power as a function of φ by comparing theoretical predictions with empirical measurements. The model was found to underestimate the power returned at medium φ (10 deg $< \varphi <$ 40 deg) when the ground surface was asphalt. The authors questioned whether it was even possible to develop better models, because of the variety of situations that might occur, e.g., metal maintenance holes on the ground increasing the reflection.

This limitation suggests that the model-derived conclusion of Ref. 18 that the flooded-to-unflooded RCS ratio should fall off very rapidly with φ may be worth further, more detailed investigation. This is the object of this paper, which carries out an empirical study on real images to examine the relationship between the ratio and φ for the case of S-1 C-band data. The study builds on the work of Ref. 23 by measuring φ to much higher accuracy than in the latter using a local high-resolution light detection and ranging (LiDAR) DSM rather than the global lower-resolution WorldDEM DSM, and also uses supervised rather than unsupervised classification.

The structure of the paper is as follows. Section 2 derives a theoretical estimation of the post- to preflood DS RCS ratio, which provides a benchmark against which empirical results can be compared. Section 3 discusses the empirical study design, whereas Sec. 4 describes the study events and data sets from the United Kingdom floods of winter 2019 to 2020. Section 5 describes the estimation of flood levels from urban DSs, based on RCS ratios at strong urban edges in the LiDAR DSM. Section 6 describes the experimental results, and Sec. 7 summarizes the conclusions.

2 Theoretical Estimation of Post- to Preflood Double Scattering Cross-Section Ratio

Double scattering caused by buildings may result from wall-ground or ground-wall scattering. In general, the high intensity of the resulting return is partly because the double scattering ray paths all have the same length, corresponding to the slant range of the base of the wall.[26]

Reference 27 used geometric optics (GO) and zero-order physical optics (PO) solutions to estimate the scattering due to a building on the ground surface. The authors showed that the double scattering contribution to the RCS is stronger than single scattering from the ground and also triple scattering contributions, so that only double scattering is considered below. In their model, the building wall is assumed to be smooth, and therefore the scattered field according to the GO approach is a plane wave propagating along the specular direction giving nonzero backscatter only for $\varphi = 0$ deg in the range 0 deg $\leq \varphi \leq$ 45 deg. The ground surface is modeled as a random rough surface with height standard deviation σ. Reference 27 points out that inclusion of ground roughness is of fundamental importance because roughness produces a non-negligible double-scattering return also for values of $\varphi > 0$, in agreement with experimental results and at variance with what is predicted by considering smooth ground. Given a radar wavenumber k, the authors point out that GO should be used to model rough ground ($k\sigma \gg 1$), and PO to model smoother ground ($k\sigma \ll 1$). For S-1 C-band radar of wavelength 6 cm, $k = 105$ m^{-1}. In an urban area, the ground surface adjacent to buildings will often be asphalt. Using the height standard deviation for asphalt of $\sigma_a = 0.0014$ m given by Ref. 18, $k\sigma = 0.15$ ($\ll 1$), which implies that the PO approach should be used to model scattering from the ground surface.

Reference 28 used the rationale developed in Ref. 27 to associate the building wall height h above the ground surface to the contribution of the double scattering to the RCS σ^0, such that

$$\sigma^0 = hf(\mathbf{p}), \tag{1}$$

where $\mathbf{p}$ is a vector of known parameters, $\mathbf{p} = (l, \sigma, L, \varepsilon_w, \varepsilon_s, \theta, \varphi)$. Here, l is the building length, L is the correlation length of the stochastic process representing the ground surface, ε_w is the

complex dielectric constant of the building wall, ε_s is the complex dielectric constant of the ground surface, and θ is the SAR incidence angle. Using the GO–PO approach

$$f(\mathbf{p}) = |S_{pq}|^2 l \tan \theta \cos \varphi \exp(-4k^2\sigma^2 \cos^2 \theta) f(\theta, \varphi, \sigma, L), \qquad (2)$$

where

$$f(\theta, \varphi, \sigma, L) = \sum_{m=1}^{\infty} ((2k\sigma \cos \theta)^{2m}/m!)(k^2L^2/4m) \exp(-(2kL \sin \theta \sin \varphi)^2/4m), \qquad (3)$$

and S_{pq} is the scattering matrix element, with p and q standing for horizontal (H) or vertical (V) polarization.[27]

In Ref. 23, both pre- and postflood S-1 images are acquired with the same radar and orbit parameters. If we assume an asphalt ground surface (σ_a^0) in the preflood image and a water surface (σ_w^0) in the postflood image, then the ratio of the double scattering RCS given as

$$r = \sigma_w^0/\sigma_a^0 = (h_A - h_W)f(\mathbf{p}_w)/((h_A - h_G)f(\mathbf{p}_a)), \qquad (4)$$

where h_A is the building wall height, h_W is the height of the floodwater, h_G is the ground height, and $\mathbf{p}_w(\mathbf{p}_a)$ is $\mathbf{p}$ for water (asphalt).

To consider the question of whether the ground around a correctly oriented building is flooded or not, Ref. 23 assumes that the flood depth is small compared with the building heights. If the depth of flooding is small, Eq. (4) reduces to

$$r \approx f(\mathbf{p}_w)/f(\mathbf{p}_a). \qquad (5)$$

If the ground is flooded, from Eq. (5), $r > 1$, whereas if it is unflooded the ratio should be 1. This is primarily because the permittivity of water is higher than that of asphalt (see table 1 of Ref. 14). Expanding Eq. (5), the RCS ratio is then

$$r \approx \frac{|S_{pq}^w|^2 \exp(-4k^2\sigma_w^2 \cos^2 \theta) f(\theta, \varphi, \sigma_w, L_w)}{|S_{pq}^a|^2 \exp(-4k^2\sigma_a^2 \cos^2 \theta) f(\theta, \varphi, \sigma_a, L_a)}, \qquad (6)$$

where S_{pq}^w and S_{pq}^a are the scattering matrix elements for water and asphalt, respectively.

Note that, from Eq. (6), if $\sigma_w = \sigma_a$ and $L_w = L_a$,

$$r \approx S_{pq}^{w2} / S_{pq}^{a2}, \qquad (7)$$

so that in this case r is independent of σ and L, and just depends on the scattering matrix elements.

The scattering matrix elements S_{VV} and S_{VH} for S-1 VV and VH polarizations, respectively, are given in table IV of Ref. 27 and are reproduced in Appendix A for convenience. They depend on θ, φ, R_{par}, R_{perp}, R_{parW}, and R_{perpW}. Here, R_{par} and R_{perp} are the Fresnel reflection coefficients of the ground [$f(\theta, \varepsilon)$, where ε = complex dielectric constant for water (ε_w) or asphalt (e_a)], and R_{parW} and R_{perpW} are the Fresnel reflection coefficients of the wall [$f(\psi, \varepsilon_W)$, where ε_W = complex dielectric constant for the wall and ψ is the incidence angle on the wall ($\psi = \cos^{-1}(\sin \theta \cos \varphi)$].

In Fig. 2, graph (a) shows the ratio r as a function of φ when $\sigma_w = \sigma_a = 0.0014$ m (from Ref. 18), and $L_w = L_a = 0.15$ m (from Ref. 28) (C-band, VV polarization). In the figure, $\theta = 35$ deg, near the center of the range for S-1. It can be seen that r is at least 8 dB over the range 0 deg $< \varphi < 30$ deg. Reference 28 states that, if the ground adjacent to the building is flooded with water, the correlation length, L, should increase and the standard deviation, σ, should decrease. Graph (b) shows the prediction when the ground is flooded so that $\sigma_w < \sigma_a$ [$\sigma_w = 0.001$ m (from Ref. 18)], when r reduces to at least 5 dB. Graph (c) shows the effect of increasing L as the ground is flooded [$L_w = 0.2$ m (from Ref. 28)] but with $\sigma_w = \sigma_a$; this leads to a steep fall in r to 3 dB at $\varphi = 12$ deg, which is a greater reduction than that which occurred when the ground roughness was reduced. Graph (d) shows the situation when $L_w = 0.2$ m and $\sigma_w = 0.001$ m, showing that r reduces to 0 dB (i.e., an intensity ratio of 1) at $\varphi = 12$ deg.
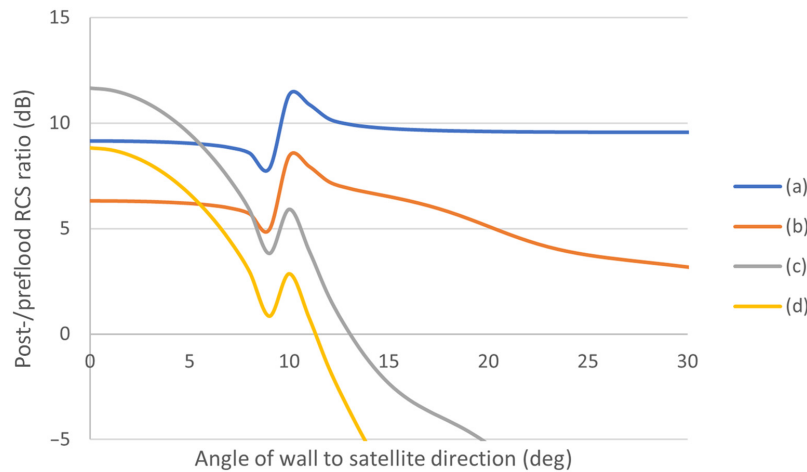
Fig. 2 Post- to preflood RCS ratio r (dB) versus angle φ, for C-band, $\theta = 35$ deg and VV polarization [Eq. (6)]. (a) $\sigma_w = \sigma_a = 0.0014$ m and $L_w = L_a = 0.15$ m. (b) $\sigma_w = 0.001$ m, $\sigma_a = 0.0014$ m, and $L_w = L_a = 0.15$ m. (c) $\sigma_w = \sigma_a = 0.0014$ m and $L_w = 0.2$ m, $L_a = 0.15$ m. (d) $\sigma_w = 0.001$ m, $\sigma_a = 0.0014$ m and $L_w = 0.2$ m, $L_a = 0.15$ m.

Graph (d) shows a situation that might occur in practice, which could imply a limitation for the method of Ref. 23 because it could only detect DS from building walls with $\varphi < 12$ deg, and there might be few of these. This is largely due to the increase in correlation length when water replaces asphalt. The model result seems extremely sensitive to correlation length. This prediction of the DS RCS ratio for C-band data is similar to that found by Ref. 18 for X-band data.

However, if the model proved not to be an accurate representation of reality, this prediction might be unduly pessimistic. For example, there might be rendering on the building walls (making them rough) or windows in the building, which might invalidate the model as the GO calculation for the reflection from the building wall assumes that the wall is smooth. Or there might have been a wind blowing when the S-1 image was acquired, so that the water was rougher and its correlation length was shorter, in which case the actual line to use might be graph (a) (which predicts a high RCS ratio over the range 0 deg $< \varphi <$ 30 deg) rather than graph (d).

Figure 3 shows the graphs of Fig. 2 for VH polarization. These have RCS ratios of zero at $\varphi = 0$ deg, have lower ratios than VV as φ increases, and show similar trends to VV, so that, for graph (d), r is only at or above 0 dB for the φ range 0 deg $< \varphi <$ 8 deg.
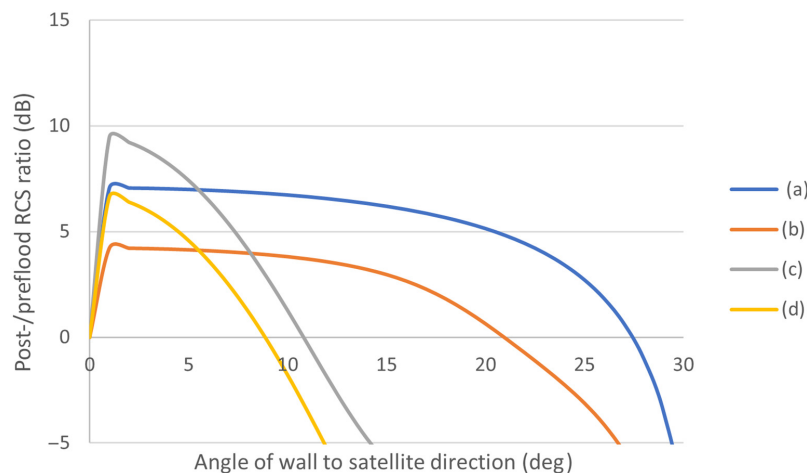

Fig. 3 Post- to preflood RCS ratio r (dB) versus angle φ, for C-band, $\theta = 35$ deg and VH polarization [Eq. (6)]. (a) $\sigma_w = \sigma_a = 0.0014$ m and $L_w = L_a = 0.15$ m. (b) $\sigma_w = 0.001$ m, $\sigma_a = 0.0014$ m and $L_w = L_a = 0.15$ m. (c) $\sigma_w = \sigma_a = 0.0014$ m and $L_w = 0.2$ m, $L_a = 0.15$ m. (d) $\sigma_w = 0.001$ m, $\sigma_a = 0.0014$ m and $L_w = 0.2$ m, $L_a = 0.15$ m.
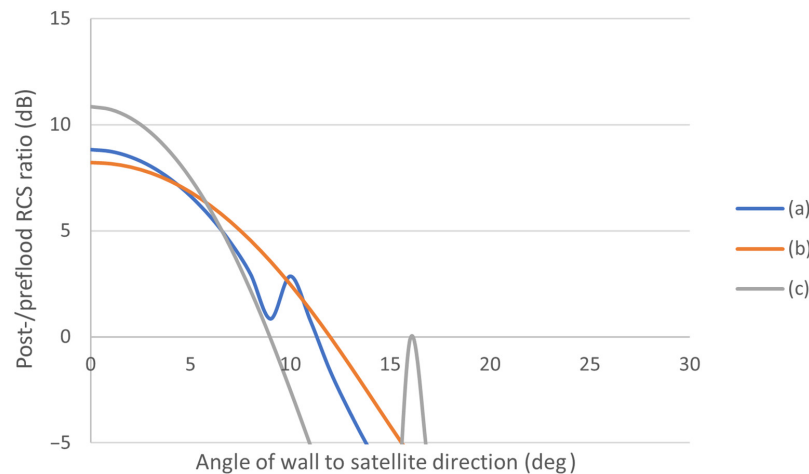
Fig. 4 Post- to preflood RCS ratio r (dB) versus angle φ, for different SAR angles θ: (a) $\theta = 35$ deg, (b) $\theta = 29.1$ deg, and (c) $\theta = 46$ deg (C-band, VV polarization) [Eq. (6)]. Parameters as for Fig. 2 graph (d), i.e., $\sigma_w = 0.001$ m, $\sigma_a = 0.0014$ m and $L_w = 0.2$ m, $L_a = 0.15$ m.

Figure 4 shows the post- to preflood RCS ratio r versus angle φ, for different SAR incidence angles θ spanning the range (29.1 deg to 46 deg) covered by the S-1 interferometric wide (IW) swath mode, the main acquisition mode over land. This is for VV polarization using the parameters of Fig. 2 graph (d). This shows that higher incidence angles give larger RCS ratios at $\varphi < 5$ deg, but also lead to ratios becoming zero at lower φ values. However, over the whole incidence angle range, flooded DS with RCS ratios greater than 0 dB are again only predicted for φ angles less than about 12 deg.

3 Empirical Study Design

In Ref. 23, urban DSs were detected using S-1 data in conjunction with the 12 m resolution WorldDEM DSM. In this study, a 2 m resolution LiDAR DSM is used instead. In practice, LiDAR would often not be available, and it might be necessary to use a lower-resolution DEM that would probably introduce some reduction in accuracy. However, this approach allows the most accurate DSM available to be used to measure φ as precisely as possible, to examine whether, for flooded DS, high RCS ratios are produced at larger φ angles. It also allows more accurate measurement of building height and length. In addition, very high-resolution optical images provided by Google Earth are used to manually check and if necessary correct the φ angles measured using LiDAR.

Sets of urban flooded and unflooded buildings are selected manually using validation data. DSs are automatically extracted from the post- and preflood SAR images for these buildings and used as training data in a supervised approach. Flooded DSs are only selected if their flood depth is less than 0.5 m, to satisfy the condition [Eq. (5)] that flood depth must be small compared with building height. This approach differs from that used in Ref. 23 where unsupervised classification was used to classify DS as flooded or unflooded prior to estimating flood levels.

4 Study Events and Data Sets

Two urban flood events from the severe flooding that occurred across the United Kingdom in winter 2019 to 2020 were studied: the Fishlake flood of November 8–20, 2019 and the Pontypridd flood of February 15–16, 2020. The Fishlake site was chosen as an example of moderate housing density and the Pontypridd site as an example of high housing density, where double scattering effects might be masked due to the presence of adjacent buildings. Further details are given in Ref. 23. An advantage of using United Kingdom events was that environment

agency LiDAR data (2 m resolution, 0.1 m height accuracy) could be obtained to estimate angle φ and building height and length accurately.

Fishlake is a village in Yorkshire, England, near the river Don downstream of Doncaster. It has a population of 700 and is surrounded by farmland. Some parts of Fishlake have high housing density (30 houses/hectare), although the average density over the whole village is 15 houses/hectare. Figure 5(a) shows LiDAR imagery of part of the urban area of Fishlake. The flooding was imaged by S-1 on November 11, 2019 and November 14, 2019 (Table 1). The SAR images were obtained on the falling limb of the hydrograph. For each image, a reference image of the unflooded area was also acquired to allow comparison between the flooded and unflooded areas. This was acquired from the same orbit with the same incidence angle, polarization, and resolution as the flooded image. A number of aerial photos showing the urban flooding were available for validation (see figure 3 of Ref. 23). According to the validation images, there was little wind present when the SAR images were acquired. Urban flood levels were estimated manually using the aerial photos in conjunction with the DSM. For the image of November 11, 2019, the flood level was 4.4 m above ordnance datum (AOD), whereas for that of November 14, 2019 the level was 4.2 m AOD.
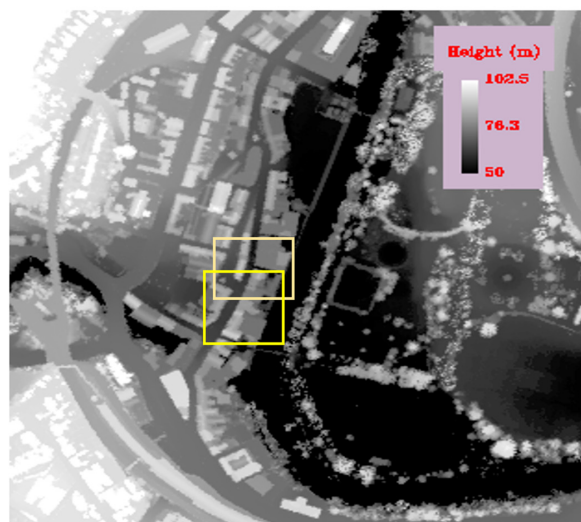
Fig. 5 LiDAR imagery of urban study sites: (a) Fishlake (53.61N, 1.01W) and (b) Pontypridd (51.60N, 3.34W). Yellow boxes mark positions of selected areas in Figs. 7 and 10.

Table 1 S-1 IW VV/VH images used for flood detection. UTC, universal time coordinated.

Site	Flood image acquisition time (UTC)	Reference image acquisition time (UTC)	Pass	Incidence angle (deg)
Fishlake (53°36′47″N, 01°00′42″W)	November 11, 2019, 17:49	October 18, 2019, 17:49	Ascending	38
	November 14, 2019, 06:14	September 15, 2019, 06:14	Descending	42
Pontypridd (51°36′01″N, 3°20′42″W)	February 16, 2020, 06:31	February 4, 2020, 06:31	Descending	34

Pontypridd is a former coal-mining town to the north of Cardiff on the river Taff in Wales, with narrow streets and dense Victorian terraced housing. It sits in a steep-sided valley. The housing density is high, being 75 houses/hectare in the east of the old town next to the river. Figure 5(b) shows LiDAR imagery of part of Pontypridd town center. Although the duration of the flooding was not long, an S-1 image was acquired at 6.31 am on February 16, 2020 (Table 1), only an hour or so after the flood peak, and validation photos were taken the same morning (see figure 4 of Ref. 23). Again the validation images indicated little wind at the time of acquisition of the SAR image. For this image, the flood level was 55.9 m AOD.

5 Estimation of Flood Levels from Urban Double Scattering

Strong edges in the LiDAR DSM were first detected using a Sobel edge detector. This calculates the magnitude and direction of the local gradient at a pixel using a 3×3-pixel window centered on the pixel. The edge thresholding selected only building walls that were greater than 3 m high. Only edges in urban areas were selected, using the World Settlement Footprint (WSF) 10 m resolution dataset.[29] Edge pixels having too large an angle φ to the satellite direction of travel were suppressed, and the range of φ values examined about the satellite look direction was limited to ± 45 deg. This was not only because a SAR image is unlikely to exhibit substantial double scattering at high φ, but also because many buildings are rectangular in plan, so that if one building wall had $\varphi > 45$ deg, the wall joining at right angles would have $\varphi < 45$ deg, so this would be examined as a potential DS instead. Nonmaxima suppression was performed in a direction perpendicular to each edge. At this stage, a brightness ratio image was also calculated from the post- and preflood images, and upscaled to the LiDAR resolution.

A connected component finder using 8-connectivity was used to label each remaining DS edge longer than 4 pixels in the LiDAR image, as such an edge should fill the majority of a 10 m S-1 pixel at least.[30] For each such edge, a straight line was fitted to its pixels to obtain a more accurate estimate of its angle φ. This angle was checked manually using aerial photos from Google Earth, and corrected if necessary. Although many buildings were rectangular, a fair proportion were houses with an extension (i.e., an addition), especially in Fishlake. In cases where the extension was at the end of the house, the house front was L-shaped, and the measurement of φ using LiDAR could be slightly wrong. The φ measured should be that of the main house front edge, not the compound edge including the house and extension. After correcting such errors, the typical error on φ was only a few degrees.

Values of the RCS ratio, the pre- and postflood brightnesses, the DSM height and the digital terrain model (DTM) height were averaged over the pixels forming the edge. This averaging was carried out for five lines all at angle φ, one along the edge of the same length as the edge, and four other similar lines displaced laterally from the edge on either side by 1 and 2 pixels. The minimum of the five DTM height averages was taken as the ground height of the DS, the maximum of the DSM averages as the building height, and maximum of the ratios (calculated from the average line brightnesses) as the DS RCS ratio. If the ground height of the DS was less than the flood level, the DS edge was marked as wet.

A regression of DS ground heights against DS RCS ratios was performed at this point, and the slope of the regression was required to be negative. The purpose of this was to check that

higher ratios were associated with lower flooded ground, rather than to remove outliers. The DS edge objects were divided into flooded and unflooded sets. For flooded objects, only those with small flooding depth (<0.5 m) were selected.

6 Results

6.1 *Initial Classification Experiments*

Reference 27 showed that, for VV polarization in C-band, there was a strong fall-off in double scattering RCS σ_0 as φ increased from 0 deg, but that σ_0 was fairly uniform over a large φ angle range for VH polarization (see figure 9 of Ref. 27). Note that this result was for the individual pre- or postflood RCS σ_0 rather than for the RCS ratio. A linear discriminant analysis was performed to estimate whether any gain would result if flooded and unflooded DSs were classified using RCS ratios from both VV and VH polarizations, rather than from VV polarization alone. The analysis was performed using training sets of DS from flooded and unflooded buildings from the Fishlake S-1 image of November 14, 2019. The discriminant analysis involved training the classifier, then reclassifying the DS with it. The Mahalanobis distance estimated using both polarizations proved to be slightly larger than that using VV polarization alone. However, the total misclassification was almost the same in both cases. While there may be a small reduction in misclassification using both polarizations, in the interest of simplicity, the analysis below has used VV alone.

In this case, training sets of flooded and unflooded buildings have been selected manually. In the normal case using test data for which class labels are unavailable, flooded and unflooded urban DS pixels can be distinguished using a threshold *ratio_thresh* on the DS RCS ratio for VV polarization. The threshold was selected using a simple two-class Bayes classifier trained on the histograms of the RCS ratios for flooded and unflooded urban DS pixels obtained from the training data.[31] Pixels from both the Fishlake S-1 images (on November 11, 2019 and November 14, 2019) were used to construct the histograms. The histograms were normalized to ensure equal prior probabilities for both classes. The minimum misclassification of flooded and unflooded DS pixels was achieved using a threshold of 2.5 dB. However, the ratio threshold was set to 3 dB to give an improved proportion of flooded to unflooded DS having ratios above the threshold. Above 3 dB, there were approximately three flooded pixels for every one unflooded pixel. The overlap between the flooded and unflooded DS RCS ratio histograms is the reason that two thresholds are used in the algorithm of Ref. 23, an upper ratio threshold above which DS is classed as flooded, and a lower ratio threshold below which DS is classed as unflooded. In addition, to distinguish it from a single scatterer, an urban DS was only considered acceptable if its preflood RCS σ_0 was greater than −11 dB, for both flooded and unflooded classes.

6.2 *Variation of RCS Ratio with Angle φ*

The results for the individual S-1 images are first considered separately to illustrate the wide range of situations that may occur. Subsequently, the results from the three scenes are combined to form an overview from which conclusions may be drawn.

6.2.1 *Fishlake flooding of November 11, 2019*

Figure 6 shows a plot of RCS ratio versus φ for flooded urban DS edges having edge lengths ≥4 pixels for the Fishlake November 11, 2019 flooding. There are 18 DS with high RCS ratios having $0 < \varphi < 10$ deg and 7 having 10 deg $< \varphi < 30$ deg, so that 28% have $\varphi > 10$ deg. So a significant proportion of DS with high RCS ratios is generated by buildings with higher φ.

Table 2 shows that the flooded DSs have a mean VV RCS ratio significantly larger than for unflooded DS. Note that the table only includes urban DS with preflood RCS $\sigma_0 > −11$ dB.

Figure 7 shows examples of DS edges with length ≥4 pixels and RCS ratio >3 dB in the flooded urban area of Fishlake, constructed from post- and preflood images using S-1 ascending
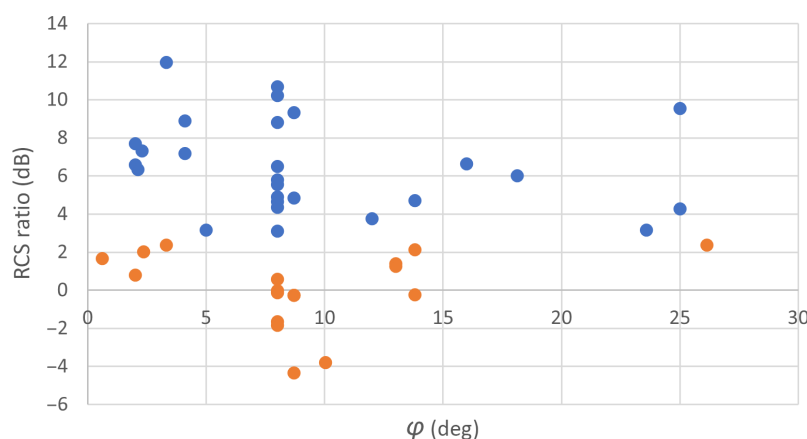
Fig. 6 Post- to preflood RCS ratio of flooded DS pixels versus φ for Fishlake November 11, 2019 flooding (VV polarization). High RCS ratios (blue) are above the 3 dB threshold, orange ratios are below.

Table 2 Means and standard deviations of flooded and unflooded urban DS for Fishlake November 11, 2019 flooding (VV polarization).

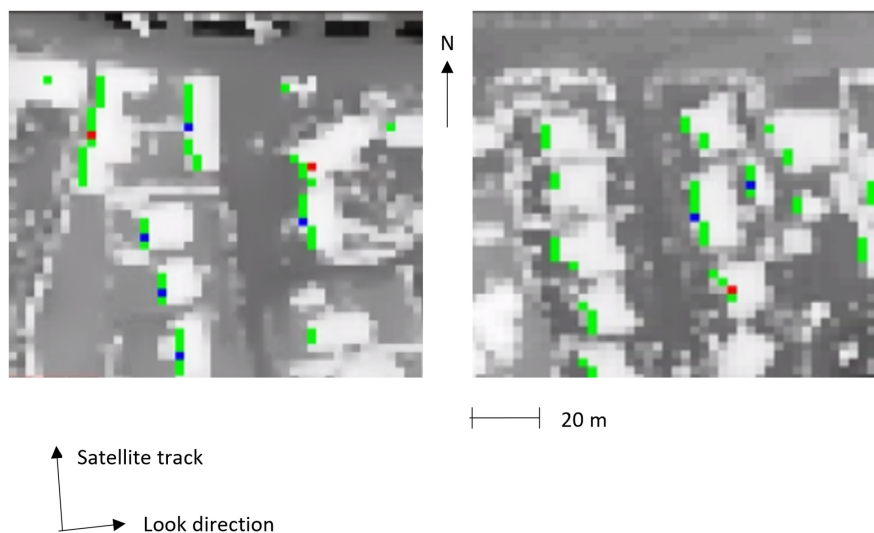| Flood state	Mean VV ratio (dB)	Standard deviation VV ratio (dB)	No. of edges
Flooded	3.9	3.8	48
Unflooded	1.4	2.3	43

Fig. 7 Examples of DSs in the flooded urban area of Fishlake constructed from post- (November 11, 2019) and preflood images (October 18, 2019), using S-1 ascending passes looking 8 deg north of east. These are superimposed on the LiDAR DSM. (Gray values = LiDAR heights, lighter = higher; green = edge in LiDAR within 30 deg of look direction (edge direction is defined as perpendicular to edge, from low to high height); edge with blue center = DS with RCS ratio >3 dB, edge length $\geq$ 4 pixels and building orientation angle φ < 10 deg, edge with red center = DS with RCS ratio > 3 dB, edge length $\geq$ 4 pixels, and φ > 10 deg. Note that several edges are <4 pixels and not considered for DS.) See Fig. 5(a) for positions of examples in main image.

Table 3 Comparison sets of data for flooded urban variables for Fishlake November 11, 2019 flooding (all samples have house heights >3 m and edge lengths ≥ 4 pixels) (VV polarization).

Comparison Set	Flooded variable	0 deg $< \varphi <$ 10 deg	10 deg $< \varphi <$ 20 deg	20 deg $< \varphi <$ 30 deg
1	DS with ratio >3 dB, high preflood σ_0	18	4	3
2	All suitable edges, with no restriction on ratio or preflood σ_0	35	14	4
3	Fraction of houses with DS of ratio >3 dB, high preflood σ_0	0.51	0.29	0.75

passes looking 8 deg north of east. These DSs include examples with $\varphi < 10$ deg and $\varphi > 10$ deg.

In Table 3, Comparison Set 1 is a histogram of the flooded data plotted in Fig. 6. This shows a peak in counts at low φ, which at first sight might be construed as predicted by graph (d) in Fig. 2. However, Comparison Set 2 in Table 3 shows the total number of houses as a function of φ, with all houses having a wall height > 3 m being considered. This is included in case there is some bias in bin counts with φ. For example, many of the houses could be aligned roughly parallel to the satellite track, so that there would be few houses at higher φ values. In the northern hemisphere, unless constrained by topography or context, many houses are built facing south, and the S-1 sensor is in polar orbit with inclination angle 98 deg, so that ascending/descending passes image the west/east walls of a house at low φ values. Similarly, in the southern hemisphere, many of the houses face north, and, in the tropics, many face east to reduce the heating effect of the sun. Comparison Set 2 shows that the majority of houses producing flooded DS has $\varphi < 10$ deg when viewed by the ascending S-1 pass looking east in Fishlake. In Comparison Set 3, the values in Comparison Set 1 are normalized by those in the equivalent φ range in Comparison Set 2, to give the fraction of houses in this range that give a ratio >3 dB. This removes the peak in counts at low φ, although the number of counts at higher φ is small. Note that the error on φ is substantially less than the 10 deg Comparison Set bin width.

Also, for the samples in Comparison Set 1, the mean ratio for $\varphi < 10$ deg $= 6.9 \pm 2.4$ while that for $\varphi > 10$ deg $= 5.4 \pm 2.2$, consistent with little fall-off with increasing φ, so that the result looks more like graph (a) in Fig. 2 than graph (d).

Another relevant question is how many buildings in the urban area that are flooded provide a DS with ratio >3 dB? From examination of the LiDAR DSM, the number of buildings in the urban area that is below the flood_level, more than 3 m high and whose area is between 16 and 100 pixels is 85. From Table 3 Comparison Set 1, the number of edges with length ≥ 4 that provide a SAR DS with ratio >3 dB in the range 0 deg $< \varphi <$ 30 deg $= 25$. So about 29% of these buildings give a high ratio DS. This may not provide a dense network of edge heights, but can be used to estimate a good average flood height for a local region.

An alternative measure DS_dens is the number of urban edges that provide a DS with ratio >3 dB and 0 deg $< \varphi <$ 30 deg per unit area. The number of flooded urban pixels in Fishlake $= 16,107 = 0.064$ km^2. So $DS\_dens = 25/0.064 = 391$ DS/km^2, in moderate density housing.

Note also that the number of flooded buildings >3 m in height with no restriction on the RCS ratio $= 53$. So $53/85 = 66\%$ of buildings >3 m in height have $0 < \varphi < 30$ deg. This means that 34% of buildings are being lost because their φ values are higher than this, or because they do not have edge lengths ≥ 4 pixels.

6.2.2 *Fishlake flooding of November 14, 2019*

In contrast to the S-1 ascending pass used to image flooding on November 11, 2019, the Fishlake flooding of November 14, 2019 was imaged on a descending S-1 pass. It might be argued that the results of the descending pass image would be correlated with those of the ascending pass image, as the same buildings are being imaged in both cases. However, the opposite sides of
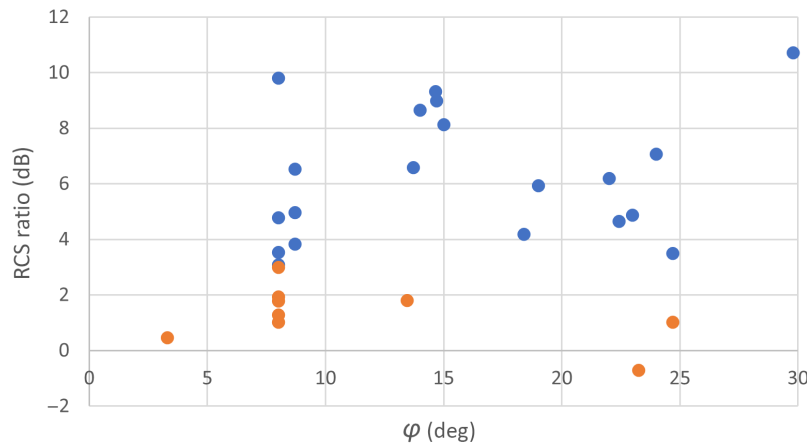
Fig. 8 Post- to preflood RCS ratio versus φ for flooded urban DS pixels for Fishlake November 14, 2019 flooding (VV polarization). High RCS ratios (blue) are above the 3 dB threshold, orange ratios are below.

the buildings are being viewed, with different ground surfaces involved. In addition, there is slightly less flooding on this later image. Consequently the descending pass results can add further useful information.

Figure 8 shows a plot of RCS ratio versus φ for flooded urban DS edges having edge lengths $\geq$ 4 pixels for the Fishlake November 14, 2019 flooding. There are flooded DS edges with high RCS ratios (>3 dB) for φ values up to 30 deg, although the sample size is small. Specifically, 7 such DSs have 0 deg < φ < 10 deg and 13 have 10 deg < φ < 30 deg, so that 65% of these DSs have φ > 10 deg. So again a significant proportion of DS edges with high RCS ratios is generated by buildings with φ > 10 deg.

Table 4 shows that flooded DSs have a mean VV RCS ratio significantly larger than that for unflooded DS. Note that the total number of edges in Table 4 differs from that in Table 2 because the opposite sides of the buildings are imaged on the ascending and descending passes.

In Table 5, Comparison Set 1 is a histogram of the flooded data plotted in Fig. 8. This appears fairly uniform, with no peak in counts at low φ as predicted by graph (d) in Fig. 2, although the

Table 4 Means and standard deviations of flooded and unflooded urban DS for Fishlake November 14, 2019 flooding (VV polarization).

Flood state	Mean VV ratio (dB)	Standard deviation VV ratio (dB)	No. of edges
Flooded	4.7	3.1	29
Unflooded	2.1	2.3	81

Table 5 Comparison sets of data for flooded urban variables for Fishlake November 14, 2019 flooding (all samples have house heights >3 m and edge lengths $\geq$ 4 pixels) (VV polarization).

Comparison Set	Flooded variable	0 deg < φ < 10 deg	10 deg < φ < 20 deg	20 deg < φ < 30 deg
1	DS with ratio >3 dB, high preflood σ_0	7	7	6
2	All suitable edges, with no restriction on ratio or preflood σ_0	11	13	11
3	Fraction of houses with DS of ratio >3 dB, high preflood σ_0	0.64	0.54	0.55

number of counts per bin is small. Comparison Set 2 in Table 5 shows the total number of houses as a function of φ, with all houses having a wall height >3 m being considered. In contrast to Comparison Set 2 of Table 3, there is no obvious bias in Comparison Set 2. Often the houses concerned are not those that produced flooded DS when Fishlake was viewed from the west on November 11, 2019. In Comparison Set 3, the values in Comparison Set 1 are normalized by those in the equivalent φ range in Comparison Set 2 to give the fraction of houses in this range that give an RCS ratio >3 dB. This again appears fairly uniform, though the number of counts is small.

Again, for the samples in Comparison Set 1, the mean RCS ratio for $\varphi < 10$ deg $= 5.2 \pm 2.3$ while that for $\varphi > 10$ deg $= 6.8 \pm 2.2$, consistent with little fall-off with increasing φ, so that the result looks more like graph (a) predicted by the model in Fig. 2 than graph (d).

From Table 5 Comparison Set 1, the number of edges with length ≥ 4 that provide a DS with ratio >3 dB in the range $0 < \varphi < 30$ deg $= 20$. Given that there are 85 relevant buildings in the flooded urban area, this means that about 23% of buildings give a high ratio DS. Again, this may not provide a dense network of DS ground heights, but can be used to estimate a good average flood height for a local region.

Also, the density of DS per unit area $DS\_dens = 20/0.064 = 312$ DS/km^2.

Note also that the number of flooded buildings >3 m in height and edge length ≥ 4 pixels with no restriction on the RCS ratio $= 35$. So only $35/85 = 41\%$ of such buildings have 0 deg $< \varphi < 30$ deg. 59% of buildings are unable to provide suitable DS because their φ values are higher than this or because they do not have edge lengths ≥ 4 pixels.

6.2.3 *Pontypridd flooding of February 16, 2020*

The Pontypridd flooding of February 16, 2020 was imaged on an S-1 descending pass at the flood peak. The houses here are generally terraced rather than detached, and the double scattering detection procedure was modified from that used for Fishlake, to split edges from long terraces of houses into sections 5 pixels long, equal to the 10 m S-1 pixel size. For each section with building height >3 m, the DS RCS ratio and φ were measured.

Figure 9 shows a plot of RCS ratio versus φ for flooded urban DS edges having edge lengths >4 pixels for the Pontypridd flooding. Three high RCS ratio DSs have $0 < \varphi < 10$ deg and five have 10 deg $< \varphi < 30$ deg, so that 63% have $\varphi > 10$ deg. So again a significant proportion of high ratios is generated by buildings with $\varphi > 10$ deg.

Table 6 again shows that flooded DSs have a mean VV RCS ratio significantly larger than that for unflooded DS.

Figure 10 shows examples of DS with edge length >4 pixels in the flooded area of Pontypridd constructed from post- (February 16, 2020) and preflood images (February 4,
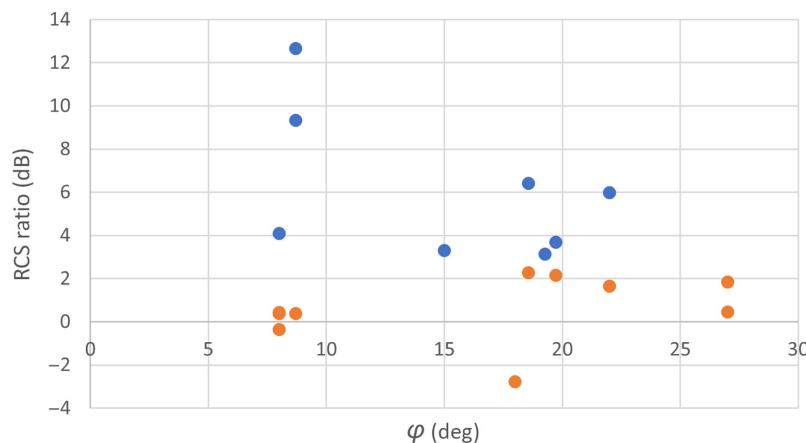

Fig. 9 Post- to preflood RCS ratio versus φ for flooded urban DS pixels for Pontypridd February 16, 2020 flooding (VV polarization). High RCS ratios (blue) are above the 3 dB threshold, orange ratios are below.

Table 6 Means and standard deviations of flooded and unflooded urban DS for Fishlake November 14, 2019 flooding (VV polarization).

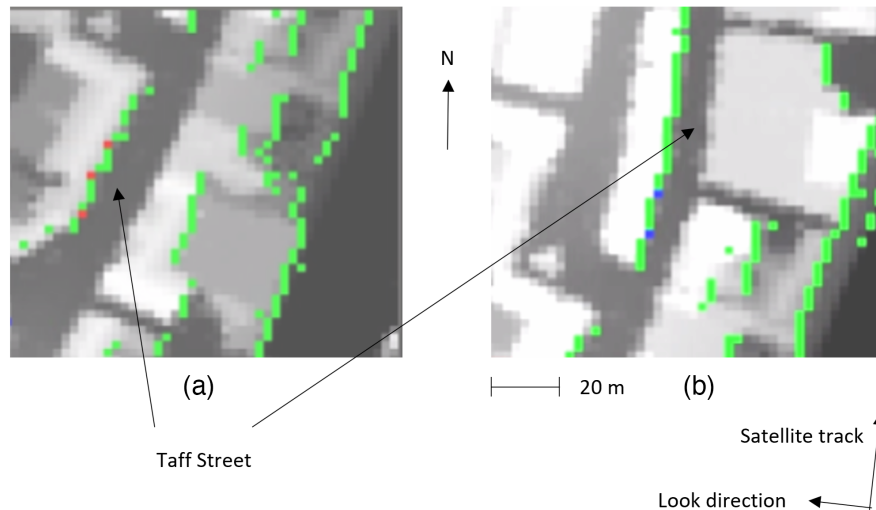| Flood state	Mean VV ratio (dB)	Standard deviation VV ratio (dB)	No. of edges
Flooded	3.0	3.5	20
Unflooded	1.5	2.6	56

Fig. 10 Examples of DSs in the flooded urban area of Pontypridd constructed from post- (February 16, 2020) and preflood images (February 4, 2020), using S-1 descending passes looking 8 deg north of west: (a) Taff Street (wider part), (b) Taff Street (narrower part). (Gray values = LiDAR heights, lighter = higher; green = edge in LiDAR within 30 deg of look direction (edge direction is defined as perpendicular to edge, from low to high height); edge with blue center = DS with RCS ratio >3 dB, edge length $\geq$ 4 pixels and building orientation angle $\varphi < 10$ deg, edge with red center = DS with RCS ratio >3 dB, edge length $\geq$ 4 pixels and $\varphi > 10$ deg. Note that several edges are <4 pixels and not considered for DS.) See Fig. 5(b) for positions of examples in main image.

2020), using S-1 descending passes looking 8 deg north of west. These are DS with RCS ratio >3 dB, and include examples with $\varphi < 10$ deg and $\varphi > 10$ deg.

In Table 7, Comparison Set 1 is a histogram of the flooded data plotted in Fig. 9. Comparison Set 2 shows that a number of buildings have walls that are again aligned roughly parallel to the satellite track, understandable as Pontypridd lies in a valley running roughly N – S. As a result, due to the topography, many houses face east or west. In Comparison Set 3, the values in Comparison Set 1 are normalized by those in the equivalent φ range in Comparison Set 2,

Table 7 Comparison sets of data for flooded urban variables for Pontypridd February 16, 2020 flooding (all samples have house heights >3 m and edge lengths $\geq$ 4 pixels) (VV polarization).

Comparison Set	Flooded variable	0 deg $< \varphi < 10$ deg	10 deg $< \varphi < 20$ deg	20 deg $< \varphi < 30$ deg
1	DS with ratio >3 dB, high preflood σ_0	3	4	1
2	All suitable edges, with no restriction on ratio or preflood σ_0	7	7	4
3	Fraction of houses with DS of ratio >3 dB, high preflood σ_0	0.43	0.57	0.25

to give the fraction of houses in this range that give an RCS ratio >3 dB. Again there is no peak in counts at low φ, though the number of counts is small.

The small number of counts in Comparison Set 1 may be due to the impact of adjacent buildings on the DS. For example, in the narrower part of Taff Street [Fig. 10(b)], the buildings on the east side of the street are putting much of the street in radar shadow. They are 12 m high roughly, and the SAR incidence angle is 34 deg, so the shadow is 8 m wide, whereas the street is only 10 m wide [Fig. 10(b), showing 2 DS with $\varphi < 10$ deg]. If the whole street was in shadow, no double scattering would be observed. However, in Fig. 10(a), where Taff Street widens to 14 m, there are 3 DS with $\varphi > 10$ deg.

For Pontypridd, the density measure DS_dens (the number of urban edges that provide a DS with ratio >3 dB with $0 < \varphi < 30$ deg per unit area) is lower than in Fishlake, probably due to the high housing density in Pontypridd. The number of flooded urban pixels in Pontypridd = 23,790 = 0.095 km^2, so that $DS\_dens = 8/0.095 = 84$ DS/km^2.

Again, for the samples in Comparison Set 1, the mean RCS ratio for $\varphi < 10$ deg = 8.7 ± 4.3 while that for $\varphi > 10$ deg = 4.5 ± 1.6, which while lower is not significantly so. Given the limited number of events, this is consistent with little fall-off with increasing φ, so that the result looks more like graph (a) in Fig. 2 than graph (d).

6.3 Combined Results

The result of combining the flooded data from all three cases in Tables 3, 5, and 7 is shown in Table 8.

A number of conclusions can be drawn from Table 8:

1. From Comparison Set 3, if the data for 10 deg < φ < 20 deg and 20 deg < φ < 30 deg are combined, then the fraction of DS with 10 deg < φ < 30 deg having high RCS ratios = 0.45 ± 0.21, which is significantly non-zero (probability > 99%), and in fact only slightly less than the fraction of DS with 0 deg < φ < 10 deg (0.53 ± 0.13). This implies that there are likely to be a significant number of flooded DSs with 10 deg < φ < 30 deg that could be distinguished in the postflood image. For the samples in Comparison Set 3, there is no significant fall-off in the mean RCS ratio as φ increases up to 30 deg, so the Comparison Set looks more like graph (a) predicted by the model in Fig. 2 than graph (d). Some support for this conclusion comes from the study of Ref. 32.

2. The predilection for building houses facing south in the northern hemisphere is apparent in the Fishlake data of November 11, 2019. As the S-1 sensor is in polar orbit with inclination angle 98 deg, descending/ascending passes image the east/west walls of a house at low φ values. Similar arguments hold in the southern hemisphere and tropics. This would favor the method of Ref. 23, as (even though there appears to be little fall-off in the mean ratio as φ increases) a low φ gives DS with high RCS ratios in flooded areas.

3. For the Fishlake data, the above two effects combine so that about 23%–29% of flooded buildings give a high ratio DS. This may not lead to a dense network of edge heights, but

Table 8 Combined comparison sets of data for flooded urban variables (all samples have house heights >3 m and edge lengths ≥4 pixels) (VV polarization).

Comparison Set	Flooded variable	0 deg < φ < 10 deg	10 deg < φ < 20 deg	20 deg < φ < 30 deg
1	DS with ratio >3 dB, high preflood σ_0	28 ± 5.3	14 ± 3.7	10 ± 3.2
2	All suitable edges, with no restriction on ratio or preflood σ_0	53 ± 7.3	34 ± 5.8	19 ± 4.4
3	Fraction of houses with DS of ratio >3 dB, high preflood σ_0	0.53 ± 0.13	0.41 ± 0.13	0.53 ± 0.21

can still be used to estimate an accurate average flood level for a local region. The same is true for the Pontypridd data, although to a lesser extent.

4. The higher housing density in Pontypridd compared with Fishlake causes DS_dens to fall in Pontypridd, probably due to the effect of adjacent buildings. For Pontypridd, $DS\_dens = 84$ DS/km^2, whereas in Fishlake $DS\_dens = 312 - 391$ DS/km^2.

7 Conclusions

This paper has taken a step toward improving urban flood detection on a global basis, using S-1 images in conjunction with WorldDEM DSM data to detect double scattering from buildings. A main conclusion is that a greater range of building orientations than predicted can contribute as DSs, thus making accurate flood detection more likely.

An empirical study has been conducted to examine the relationship between the flooded-to-unflooded DS RCS ratio and angle φ. This shows that S-1 VV polarization is better than VH polarization for discriminating flooded and unflooded DS using RCS ratios, as found by Ref. 21 (see Sec. 6.1). The theoretical model used predicts that, for C-band VV data, the ratio of the flooded-to-unflooded DS RCS should be high at $\varphi = 0$ deg but only small at $\varphi > 10$ deg, implying that few DSs may be detected in an urban area. However, the study of real images clearly shows that the model tends to underestimate the number of DS with high RCS ratios in the φ range 10 deg $< \varphi <$ 30 deg. We also note that building orientation preference can in some circumstances lead to a preponderance of buildings with low φ. Most significantly, we conclude that sufficient DS ground heights can be determined in an urban area to estimate an accurate local average flood level, although in high density housing there are less of these due to the presence of adjacent buildings.

It was shown in Ref. 23 that the method described there was able to identify sufficient DSs to detect flooding at high resolution in urban areas on a global basis using S-1 SAR and WorldDEM DSM data. What Ref. 23 did not make clear was why sufficient DSs could be detected. Due to the low resolution of WorldDEM, φ could not be determined sufficiently accurately to decide whether simply by chance most of the flooded building edges had 0 deg $< \varphi <$ 10 deg (giving DS with high RCS ratios), or whether the theoretical scattering models were underestimating the number of flooded DS with high ratios having 10 deg $< \varphi <$ 30 deg. By its use of high-resolution LiDAR data to measure φ accurately, this paper has been able to show that the latter is true. This gives confidence in the ability of the method described in Ref. 23 to identify sufficient DSs to detect urban flooding. Furthermore, it gives confidence in the ability of high and very high-resolution SARs in general (in conjunction with high-resolution DSMs) to detect urban flooding using double scattering, which is significant given that SAR is becoming ever more employed as a tool for the rapid detection of flooding.

8 Appendix A: Scattering Matrix Element Calculations

The scattering matrix elements S_{VV} and S_{VH} for S-1 VV and VH polarizations, respectively, are given in table IV of Ref. 27, and depend on θ, φ, R_{par}, R_{perp}, R_{parW}, and R_{perpW}. Here, R_{par} and R_{perp} are the Fresnel reflection coefficients of the ground [$f(\theta, \varepsilon)$, where ε = complex dielectric constant for water (ε_w) or asphalt (ε_a)], and R_{parW} and R_{perpW} are the Fresnel reflection coefficients of the wall [$f(\psi, \varepsilon_{Wall})$, where ε_{Wall} = complex dielectric constant for the wall and ψ is the incidence angle on the wall ($\psi = \cos^{-1}(\sin \theta \cos \varphi)$]

$$S_{VV} = A_V[\sin^2 \theta \sin 2\varphi + R_{perp}(\theta) \sin 2\varphi (1 + \cos^2 \theta)] + 2B_V R_{par}(\theta) \cos \theta \cos 2\varphi,$$

$$S_{VH} = A_V[-2R_{perp}(\theta) \cos \theta \cos 2\varphi] + B_V[\sin^2 \theta \sin 2\varphi + R_{par}(\theta) \sin 2\varphi (1 + \cos^2 \theta)],$$

where

$$A_V = -(R_{perpW}(\psi) + R_{parW}(\psi)) \cos \theta \cos \varphi \sin \varphi,$$
$$B_V = -R_{perpW}(\psi) \sin^2 \varphi + R_{parW}(\psi) \cos^2 \theta \cos^2 \varphi, \tag{8}$$

and the Fresnel amplitude reflection coefficients are given as

$$R_{\text{parW}} = ((\varepsilon_{\text{Wall}} - \sin^2 \psi)^{0.5} - \varepsilon_{\text{Wall}} \cos \psi)/((\varepsilon_{\text{Wall}} - \sin^2 \psi)^{0.5} + \varepsilon_{\text{Wall}} \cos \psi)),$$
$$R_{\text{perpW}} = (\cos \psi - (\varepsilon_{\text{Wall}} - \sin^2 \psi)^{0.5})/(\cos \psi + (\varepsilon_{\text{Wall}} - \sin^2 \psi)^{0.5}),$$
$$R_{\text{par}} = ((\varepsilon - \sin^2 \theta)^{0.5} - \varepsilon \cos \theta)/((\varepsilon - \sin^2 \theta)^{0.5} + \varepsilon \cos \theta)),$$
$$R_{\text{perp}} = (\cos \theta - (\varepsilon - \sin^2 \theta)^{0.5})/((\cos \theta + (\varepsilon - \sin^2 \theta)^{0.5}), \tag{9}$$

where for unflooded ground $\varepsilon = \varepsilon_a$, and for flooded ground $\varepsilon = \varepsilon_w$ (see Ref. 33, remembering that $\varepsilon = n^2$ (n = refractive index)).

Acknowledgments

Code and Data

The S-1 and LiDAR data used in the study are both open access (see Refs. 34 and 35, respectively).

References

1. H. C. Winsemius et al., "Global drivers of future river flood risk," *Nat. Clim. Change* **6**, 381–385 (2015).
2. Y. Li et al., "Urban flood mapping using SAR intensity and interferometric coherence via Bayesian network fusion," *Remote Sens.* **11**(19), 2231–2252 (2019).
3. M. Pitt, "Learning lessons from the 2007 floods," U.K. Cabinet Office Report, 2008, http://archive.cabinetoffice.gov.uk/pittreview/thepittreview.html.
4. J. Garcia-Pintado et al., "Satellite-supported flood forecast in river networks: a real case study," *J. Hydrol.* **523**, 706–724 (2015).
5. L. Giustarini et al., "Probabilistic flood mapping using synthetic aperture radar data," *IEEE Trans. GeoSci. Remote Sens.* **54**(12), 6958–6969 (2016).
6. R. Hostache et al., "Near-real-time assimilation of SAR-derived flood maps for improving flood forecasts," *Water Resour. Res.* **54**(8), 5516–5535 (2017).
7. E. S. Cooper et al., "Observation operators for assimilation of satellite observations in fluvial inundation forecasting," *Hydrol. Earth Syst. Sci.* **23**, 2541–2559 (2019).
8. S. Grimaldi et al., "Sensing-derived water extent and level to constrain hydraulic flood forecasting models: opportunities and challenges," *Surv. Geophys.* **37**, 977–1034 (2016).
9. E. Nemni et al., "Fully convolutional neural network for rapid flood segmentation in synthetic aperture radar imagery," *Remote Sens.* **12**, 2532 (2020).
10. Copernicus Emergency Management Service, "GloFAS Global Flood Monitoring (GFM)," 2021, https://www.globalfloods.eu/technical-information/glofas-gfm/
11. R. Hostache et al. "A first evaluation of the future CEMS systematic global flood monitoring product," 2021, https//events.ecmwf.int/event/222/contributions/2274/attachments/1280/2347/Hydrological-WS-Hostache.pdf.
12. D. C. Mason et al., "Flood detection in urban areas using TerraSAR-X," *IEEE Trans. Geosci. Remote Sens.* **48**(2), 882–894 (2010).
13. D. C. Mason et al., "Near real-time flood detection in urban and rural areas using high resolution synthetic aperture radar images," *IEEE Trans. Geosci. Remote Sens.* **50**(8), 3041–3052 (2012).
14. D. C. Mason et al., "Detection of flooded urban areas in high resolution synthetic aperture radar images using double scattering," *Int. J. Appl. Earth Obs. Geoinf.* **28C**, 150–159 (2014).

15. D. C. Mason et al., "A robust algorithm for detecting floodwater in urban areas using synthetic aperture radar images," *J. Appl. Remote Sens.* **12**(4), 045011 (2018).
16. M. Tanguy et al., "River flood mapping in urban areas combining RADARSAT-2 and flood return period data," *Remote Sens. Environ.* **198**, 442–459 (2017).
17. L. Giustarini et al., "A change detection approach to flood mapping in urban areas using TerraSAR-X," *IEEE Trans. Geosci. Remote Sens.* **51**(4), 2417–2430 (2013).
18. L. Pulvirenti et al., "Use of SAR data for detecting floodwater in urban and agricultural areas: the role of interferometric coherence," *IEEE Trans. GeoSci. Remote Sens.* **54**(3), 1532–1544 (2016).
19. M. Chini et al., "Sentinel-1 InSAR coherence to detect floodwater in urban areas: Houston and hurricane Harvey as a test case," *Remote Sens.* **11**(2), 107 (2019).
20. Y. Li, S. Martinis, and M. Wieland, "Urban flood mapping with an active self-learning convolutional neural network based on TerraSAR-X intensity and interferometric coherence," *ISPRS J. Photogramm. Remote Sens.* **152**, 178–191 (2019).
21. H. Zhang et al., "An urban flooding index for unsupervised inundated urban area detection using Sentinel-1 polarimetric SAR images," *Remote Sens.* **13**, 4511 (2021).
22. Y. N. Lin et al., "Urban flood detection with Sentinel-1 multi-temporal synthetic aperture radar (SAR) observations in a Bayesian framework: a case study for Hurricane Matthew," *Remote Sens.* **11**, 1778 (2019).
23. D. C. Mason, S. L. Dance, and H. L. Cloke, "Floodwater detection in urban area using Sentinel-1 and WorldDEM data," *J. Appl. Remote Sens.* **15**(3), 032003 (2021).
24. Y. Dong, B. Forster, and C. Ticehurst. "Radar backscatter analysis for urban environments," *Int. J. Remote Sens.* **18**(6), 1351–1364 (1997).
25. A. Ferro et al., "On the relationship between double bounce and the orientation of buildings in VHR SAR images," *IEEE Trans. Geosci. Remote Sens. Lett.* **8**(4), 612–616 (2011).
26. G. Franceschetti et al., "SAR raw signal simulation for urban structures," *IEEE Trans. Geosci. Remote Sens.* **41**(9), 1986–1995 (2003).
27. G. Franceshetti, A. Iodice, and D. Riccio, "A canonical problem in electromagnetic backscattering from buildings," *IEEE Trans. Geosci. Remote Sens.* **40**(8), 1787–1801 (2002).
28. P. Iervolini et al., "Flooding water depth estimation with high-resolution SAR," *IEEE Trans. GeoSci. Remote Sens.* **53**(5), 2295–2307 (2015).
29. M. Marconcini et al., "Outlining where humans live, the World Settlement Footprint 2015," *Sci. Data* **7**, 242 (2020).
30. L3Harris Geospatial Solutions, "LABEL_REGION," 2022, https://www.l3harrisgeospatial.com/docs/label_region.html.
31. R. O. Duda and P. E. Hart, Pattern Classification and Scene Analysis, Wiley, New York (1973).
32. Y. J. Kwak, R. Natsuaki, and S. H. Yun, "Effect of building orientation on urban flood mapping using ALOS-2 amplitude images," in *38th IGARSS Symp.*, pp. 2350–2353 (2018).
33. Wikipedia, "Fresnel equations," 2023, https://en.wikipedia.org/wiki/Fresnel_equations.
34. Copernicus, "Copernicus open access hub," 2023, https://scihub.copernicus.eu/.
35. Defra, "Defra survey data download," 2023, https://environment.data.gov.uk/DefraDataDownload/?Mode=survey.

David C. Mason received his BSc and PhD degrees in physics from Imperial College, University of London. He is a senior research fellow in the Department of Geography and Environmental Science at the University of Reading, United Kingdom. His current research interest is the use of remote sensing in hydrology, in particular using SAR flood extents for emergency flood relief management and improved flood inundation forecasting, and SAR soil moisture for improved hydrologic modeling.

Sarah L. Dance received her PhD from the Division of Applied Mathematics at Brown University, United States, in 2002. She is a professor of data assimilation at the University of Reading, United Kingdom, jointly held in the Department of Mathematics and Statistics and the Department of Meteorology. She recently co-directed the UK NERC Flooding from Intense Rainfall program and holds an EPSRC Senior Fellowship in Digital Technology for Living with Environmental Change.

Hannah L. Cloke received her BSc and PhD degrees in geography from the University of Bristol, United Kingdom, in 1999 and 2003, respectively. She is a professor of hydrology at the University of Reading, United Kingdom, and a guest professor at Uppsala University, Sweden. Her current research focuses on the theoretical and practical development of early warning systems for natural hazards, particularly for floods, and disaster risk management, for which she was awarded the Plinius Medal of the European Geosciences Union in 2018.